

Geophysical Research Letters®



RESEARCH LETTER

10.1029/2023GL106422

Key Points:

- The inventories with over 21 years of continuous landslide activities prior to and following the Wenchuan earthquake were compiled
- Apart from acknowledged attenuation, diverse environment exposed various evolutionary patterns of post-earthquake landslide activity
- Damaged plant succession and ecological function restoration underwent lengthier durations than post-seismic landslide stabilization

Supporting Information:

Supporting Information may be found in the online version of this article.

Correspondence to:

X. Fan,
fxm_cdut@qq.com

Citation:

Wang, X., Fan, X., Fang, C., Dai, L., Zhang, W., Zheng, H., & Xu, Q. (2024). Long-term landslide evolution and restoration after the Wenchuan earthquake revealed by time-series remote sensing images. *Geophysical Research Letters*, 51, e2023GL106422. <https://doi.org/10.1029/2023GL106422>

Received 15 SEP 2023

Accepted 15 JAN 2024

Author Contributions:

Conceptualization: Xin Wang, Xuanmei Fan

Data curation: Xin Wang, Chengyong Fang, Wei Zhang

Formal analysis: Xin Wang, Lanxin Dai

Funding acquisition: Xin Wang, Xuanmei Fan

Investigation: Xuanmei Fan, Chengyong Fang, Lanxin Dai

Methodology: Xin Wang, Hongrui Zheng

Project administration: Xuanmei Fan



Resources: Chengyong Fang

Supervision: Xuanmei Fan, Qiang Xu

© 2024. The Authors.

This is an open access article under the terms of the [Creative Commons Attribution-NonCommercial-NoDerivs License](#), which permits use and distribution in any medium, provided the original work is properly cited, the use is non-commercial and no modifications or adaptations are made.

Long-Term Landslide Evolution and Restoration After the Wenchuan Earthquake Revealed by Time-Series Remote Sensing Images

Xin Wang¹ , Xuanmei Fan¹ , Chengyong Fang¹, Lanxin Dai¹, Wei Zhang², Hongrui Zheng³, and Qiang Xu¹

¹State Key Laboratory of Geohazard Prevention and Geoenvironment Protection, Chengdu University of Technology, Chengdu, China, ²National Key Laboratory of Water Disaster Prevention, Nanjing Hydraulic Research Institute, Nanjing, China, ³School of Geoscience and Technology, Southwest Petroleum University, Chengdu, China

Abstract A powerful earthquake, particularly in mountainous regions, has the ability to trigger an immense number of landslides, resulting in severe damages. However, effectively assessing their recoveries in the years following the mainshocks has not yet been attempted due to the lack of continuously updated landslide inventories. Therefore, we proposed a novel detection framework utilizing time-series Landsat images from 2000 to 2021, which enabled us to achieve a long-term landslide inventory in the seismic zone for the first time. The response patterns of landslide development under different conditions were explored in detail. The restoration models were quantitatively established, revealing that the recoveries of post-earthquake landslide activity and vital environmental indicators require a range from ~5.29 to ~25.00 years. This pioneering research is highly beneficial in comprehending the impact of earthquake-induced hazards on short-term land surface damage and long-term ecological equilibrium.

Plain Language Summary The Wenchuan earthquake triggered tens of thousands of landslides and caused severe surface damages, leading to adverse impacts on the local environment in the following period. Therefore, we implemented an approach that combines change detection techniques with long-term remote sensing images to track the landslide activities from 2000 to 2021. Consequently, continuous landslide maps have been produced, and the post-earthquake landslide activities were analyzed under different conditions considering various factors. We also explored the restorations for the undisturbed landslides after the earthquake using important ecological indicators. The results suggest that the recovery of landslide activity and surface evapotranspiration was rapid. However, the regrowth and succession of damaged plants required a longer time. Moreover, it would take decades to fully restore the vegetation ecological function, which shatters our original impression on the persistence of post-earthquake landslide impacts.

1. Introduction

Landslides refer to the rapid mass wasting of bedrock, soil, and debris down a slope, causing severe casualties and economic losses (Cruden, 1991; Korup et al., 2010). The catastrophic earthquakes in mountainous regions are the major triggers of extensive co-seismic landslides (Guzzetti et al., 1999). The deposits confined on hillslopes offer an abundant source of materials and are therefore prone to collapse or liquefy with a loss of suction or an increase of pore water pressure (Hu et al., 2018). Debris extension and remobilization may occur multiple times under external forces such as aftershocks, rainfall, snowmelt, and anthropogenic disturbances, posing additional threats to earthquake-affected areas (Fan, Scaringi, Domènech, et al., 2019; Fan, Scaringi, Korup, et al., 2019; Hovius et al., 2011; LaHusen et al., 2020). Due to their impacts on ecological components, including changes in landscape and landform, surface and subsurface runoff, vegetation growth, post-earthquake landslides can lead to unprecedented disturbances to local ecosystems (Rasigraf & Wagner, 2022; Sidle & Bogaard, 2016). Environmental damage is bound to result in energy imbalances, which are embodied in unstable deposits, barrier dams, and accelerating slopes, further contributing to susceptible landslides in turn (Fan et al., 2021; Fan, Scaringi, Domènech, et al., 2019; Fan, Scaringi, Korup, et al., 2019; G. K. Li & Moon, 2021). Under the repeated adjustment of geological stress and self-repair of ecological structure, landslide activities as well as ecosystem functions can be restored to stabilization (Marc et al., 2015; Tanyaş et al., 2021). Therefore, clarifying the evolution patterns of post-earthquake landslides and understanding the ecological restoration, which are still the challenges, are crucial for secondary geohazard prevention and post-disaster reconstruction.

Validation: Xin Wang, Chengyong Fang, Lanxin Dai

Visualization: Xin Wang, Wei Zhang, Hongrui Zheng

Writing – original draft: Xin Wang

Writing – review & editing:

Xuanmei Fan, Qiang Xu

Earth observations through remote sensing possess the ability of large area coverage and short revisit interval, providing a great opportunity to monitor land surface disturbances initiated by geohazards in wide geographical ranges compared to time and labor costly in-situ investigations (Metternicht et al., 2005; Van Westen et al., 2008). In light of this, many studies have focused on Wenchuan earthquake-triggered landslides based on remote sensing technology. Some researches mapped multi-temporal post-earthquake landslides by integrating field investigations and image interpretation in an attempt to discover their evolution patterns (Chen et al., 2020; Fan et al., 2021; Kinsey et al., 2021; Tang et al., 2016). Other studies acquired information about these activities via monitoring the vegetation damaged by post-earthquake landslides (Lin et al., 2005; Shen et al., 2020; Yang et al., 2018; Yunus et al., 2020). While these accomplishments allow for the estimation of the preliminary stages of post-earthquake landslides, the subsequent apparent deficiencies necessitate further attention. First, the inventories used for post-earthquake landslide analysis are discrete and isolated, which pose considerable uncertainty and bias for their continuous changes. Furthermore, the time spans considered for post-earthquake landslides in current researches are insufficient, leading to irresponsible estimation of landslide development. Lastly, no comprehensive evaluation and prediction of the long-term impacts of earthquake-triggered landslides on local ecosystems have been attempted thus far.

To further fill the knowledge gaps impeded by these limitations, we proposed a novel time-series landslide detection approach for the first attempt, which realized the mapping of continuous landslide distribution before and after the Wenchuan earthquake. The detailed evolution patterns of post-earthquake landslides are accurately depicted, and the long-term restoration of landslide activities and local ecology after the earthquake were quantitatively assessed. These investigations expound a complete course of a major earthquake-induced landslides and contribute to a comprehensive assessment of post-disaster environment evolution.

2. Study Area

The Mw 7.9 Wenchuan earthquake struck the Longmen Mountains at the eastern margin of Qinghai-Tibet Plateau on 12 May 2008, with the focus located at latitude 31.00°N and longitude 103.32°E around 19 km depth (Figure 1) (Huang & Fan, 2013). This region is renowned for its dynamic tectonic activity. A consequence of collisions between the Indian and Eurasian plates led to four major faults: Wenchuan-Maowen Fault, Beichuan-Yingxiu Fault (BYF), Pengguan Fault, and Qingchuan Fault (Dai et al., 2011). The earthquake instigated extensive landslides, topographical modifications, surface deformations and ruptures, resulting in severe damage to ecological environment.

3. Data and Methods

3.1. Data Sources

As our objective was to systematically explore the landslide activities prior to and following the Wenchuan earthquake, the long-term dense Landsat image series were employed to collect intensive and continuous observations. The surface reflectance data of Landsat were obtained from Google Earth Engine, a cloud-based geospatial analysis platform with immense storage and computational capabilities (Gorelick et al., 2017). Eight bands of each image, comprising of six spectral, one thermal, and one quality assessment band, were adopted for landslide detection. Quality assessment was carried out using Function of Mask (FMask) to ensure that outliers such as fill, cloud, and cloud shadow were identified, leaving behind clear observations (Zhu et al., 2015). The Landsat data encompassed the time period from 1 January 2000 to 31 December 2021, thus enabling long-term monitoring of post-earthquake landslide recovery as well as pre-earthquake landslide activity. A total of 521 images were exploited with 123, 251, and 147 from Landsat 5, 7, and 8, respectively. The images were evenly dispersed across all seasons, providing a suitable condition for harmonic function fitting with seasonal components (methodology details in Section 3.2). The overall distribution of time-series Landsat observations is depicted in Figure S1 of Supporting Information S1.

To investigate the post-earthquake landslide evolution under the influence of topographic, seismic, lithologic, and climatic factors, auxiliary data sets including digital elevation model (DEM), lithology, peak ground acceleration (PGA) and velocity (PGV), land surface temperature (LST), and precipitation were acquired. Furthermore, crucial indicators of ecological environment, such as evapotranspiration (ET), leaf area index (LAI), enhanced vegetation index (EVI), gross primary productivity (GPP), and net primary productivity (NPP), were also

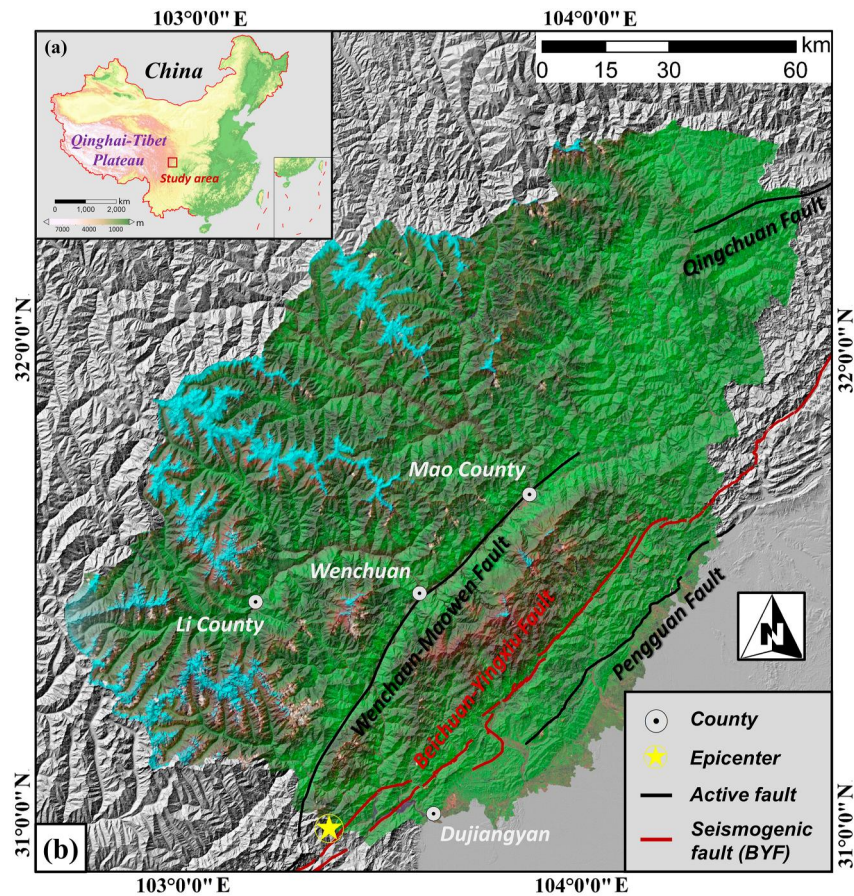


Figure 1. Background of the study area. (a) Topographic map of China. (b) False color composite image from Landsat 8 (acquired on 4 June 2021), accompanied by seismotectonic information.

obtained to enable a qualitative leap from continuous monitoring of landslides to long-term ecological effects. The details of these data sets are listed in Table S1 and S2 of Supporting Information S1.

3.2. Methods

An earthquake not only triggers co-seismic landslides, but also induced post-seismic deposit failures on co-seismic debris after the event (Tang et al., 2016; S. Zhang & Zhang, 2017). These landslides lead to sudden land surface disturbances, which can be recorded by remote sensing through change analysis. Continuous change detection and classification (CCDC) through time-series remote sensing images were therefore adopted to fully understand the landslides activities over 21 years. CCDC assembles all available Landsat observations for each pixel to estimate time-series models combining seasonal and trend components as Equation 1, which are, in turn, employed to predict future observations (Zhu & Woodcock, 2014).

$$P(i, d) = a_i + b_i^1 \cos\left(\frac{2\pi d}{T}\right) + b_i^2 \sin\left(\frac{2\pi d}{T}\right) + c_i d \quad (1)$$

where $P(i, d)$ is the predict observation at Landsat band i on Julian day d . a_i and c_i are the coefficients of trend component, whereas b_i^1 and b_i^2 are the coefficients of seasonal component. T is the average days of a year (365.25). The model can be executed once 15 clear observations are available for initialization, out of which the first 12 observations are used for constructing the model outline, and the remaining observations are selected for examining whether the land cover has undergone any changes. Considering the differences between model predictions and observations for a stable land cover follow the normal distribution with the standard deviation of Root Mean Square Error (RMSE), the thresholds are defined based on the change probability of 0.99. In other

words, the spectral signals usually deviate from model predictions by more than three times the RMSE when land cover change occurs (Zhu & Woodcock, 2014). Hence, the algorithm averages the discrepancies between observations and model predictions that have been normalized by three times the RMSE for all the Landsat bands (Equation 2).

$$D = \frac{1}{k} \sum_{i=1}^k \frac{|O(i,d) - P(i,d)|}{3 \times \text{RMSE}_i} \quad (2)$$

where D is the average difference between prediction and observation. k is the number of Landsat bands, and $O(i,d)$ is the observed data. Consequently, if their difference exceeds 1, it can be inferred that the land cover has undergone a change, and vice versa.

However, other natural and anthropogenic disturbances such as residential construction, deforestation, and flood also lead to changes in land cover. To screen out the landslides from them, time-series land cover needs to be achieved for further discrimination, which can also be performed via CCDC. Due to the diverse temporal characteristics of land covers, a supervised classifier that incorporates time-series model coefficients and training samples can be utilized for classification, whose classification system and acquisition procedure are illustrated in Text S1 and Table S3 in Supporting Information S1. Support Vector Machine, Random Forest, Rotation Forest, and K-Nearest Neighbor are integrated to enhance the reliability and robustness of CCDC, in which majority voting is carried out to achieve the most frequent results of classified land covers for each pixel over a given period (Wang et al., 2022). It is worth noting that over 99% of the landslides in the study area are located far away from settlements and are covered by vegetation more or less after an event. Therefore, they can be distinguished by identifying situations where the land cover is transformed to vegetation (grass and forest).

In addition to accomplishing the recognition of long-term continuous landslides, it holds immense importance to delve deeper into the evolution of landslide activities and the restoration of the ecological environment after the earthquake. Considering that land surface damages caused by post-earthquake landslides recovered at a decaying rate until stabilization, an exponential function (Viedma et al., 1997) is employed to establish a recovery model based on annual post-earthquake landslide detection and vital ecological indicators as shown in Equation 3.

$$R = R_0 + p \times e^{qt} \quad (3)$$

where R is the predict indicators on year t . R_0 is the indicator with the max/min value, (i.e., the limiting value of the indicator at infinite t). p is the indicator variation between the earthquake immediately happened and long period after, and is well related to the target properties. q is expressed in units of time, which determines the recovery speed. To avoid interference from other factors, the post-earthquake landslide achievements were taken into account. Hence, the following two situations are concerned. For a co-seismic landslide that did not experience reactivation, the tracking span of the restoration ranges from the first year after the earthquake to the end of the effective observations. Otherwise, the record spans from the first year after the earthquake to the last year before reactivation.

4. Results and Discussion

4.1. Long-Term Continuous Landslide Recognition

The long-term continuous landslide distribution from 2001 to 2021 was achieved as Figure 2a. Since at least 12 clear observations before the earthquake are necessary for co- and post-seismic landslide detection according to the algorithm, we also calculated the pre-event data availability of each pixel (Figure S2 in Supporting Information S1). To prove the recognition accuracy, an inventory combining previous achievements of the Wenchuan earthquake-induced landslides and additional manual interpretations was adopted as reference (Fan, Scaringi, Domènech, et al., 2019; Fan, Scaringi, Korup, et al., 2019). The overall accuracy, F1-score, and Kappa coefficient reach 80.40%, 0.60, and 0.47, respectively, indicating comprehensive high accuracy and consistency. They provide a commission error of 12.24%, demonstrating the designed framework is capable of predominantly avoiding from categorizing other types of land cover changes as landslides. While the omission error is higher (41.26%), since some of small-size landslides, which encompass the areas less than the pixel size of Landsat

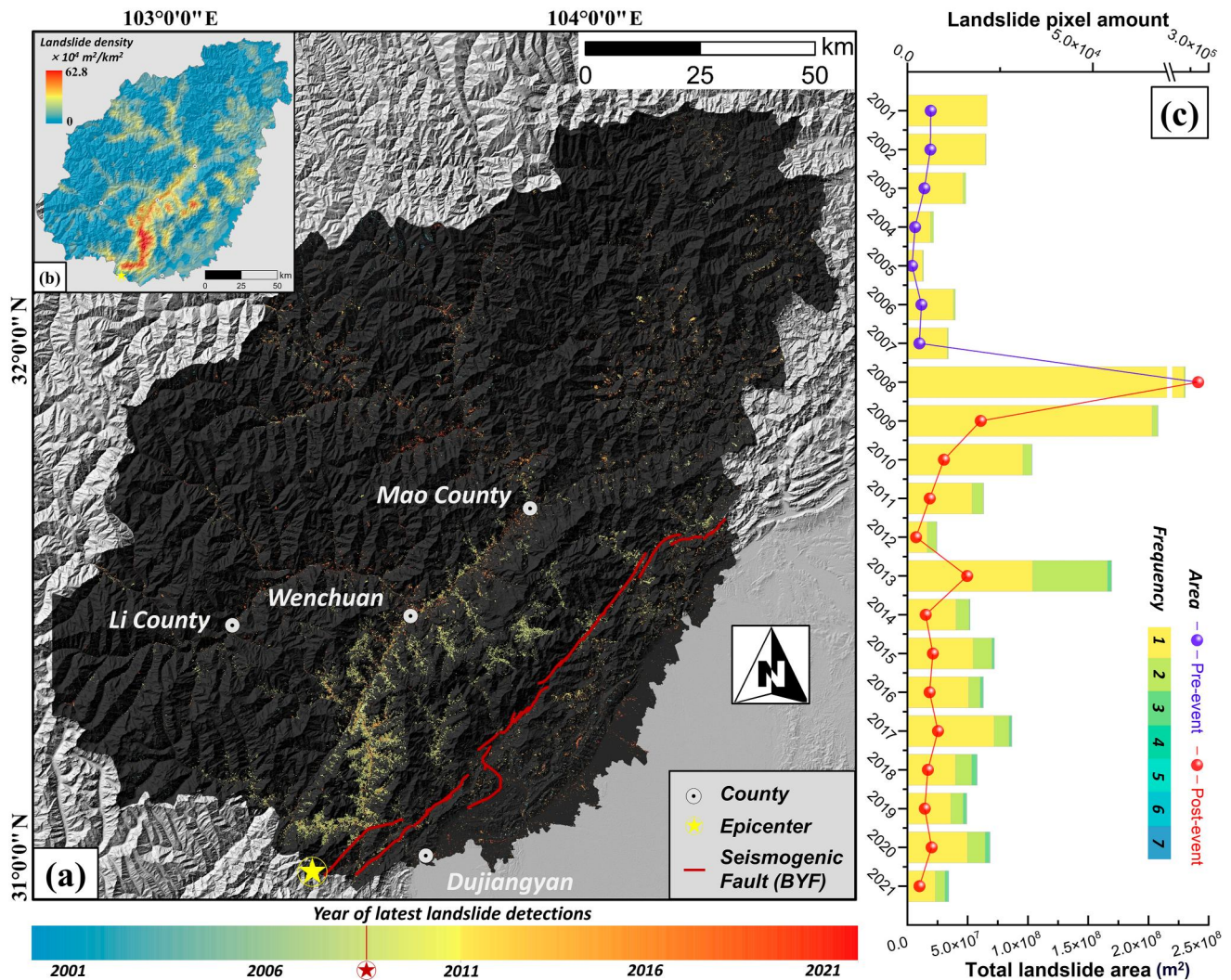


Figure 2. Long-term continuous landslide achievements from 2001 to 2021. (a) Landslides with the latest detections via time-series remote sensing images. (b) Spatial distribution of accumulated landslide density. (c) Statistics of annual landslide area and frequency.

images (900 m²), were not fully recognized. Detailed assessments are provided in Figure S3 in Supporting Information S1. The above results demonstrate the effectiveness and reliability of the proposed framework in time-series landslide detection. Figure S4 in Supporting Information S1 exemplifies five subsets with Landsat 5 images and the corresponding detected landslides.

Most landslides are concentrated along the hanging wall of the seismogenic fault (BYF), confirming the hanging wall effect of thrust fault seismicity. Figure 2b indicates accumulated landslide density, with the maximum close to the epicenter reaching 0.63 km²/km². The overall landslide area spans 580.28 km², accounting for 3.20% of the entire region. Among these landslides, 48.50 km² occurred more than once, accounting for 8.36% of the total landslide area. Figure 2c summarizes annual landslides (line graph) and further refines their frequency (bar graph). The annual activity remained stable before 2008, but increased sharply in the year of the Wenchuan earthquake, inducing a landslide area of 241.29 km² (occupying 41.58% of the total landslide area over 21 years). As time passed, landslide activities decreased while the proportion of multiple landslide events inversely increased, ultimately returning to stabilization. Note that there was a peak of landslides in 2013, in which the proportion of reactivation reached 38.72%. According to the position and time of detected landslides, it was found that heavy rainfall with a return of over 100 years attacked near the epicenter, leading to extensive resurrection and extension of co-seismic landslides and debris flows (Yin et al., 2016; S. Zhang & Zhang, 2017). There is no doubt that the landslide activity was prolonged in these influenced catchments. But fortunately, in time series

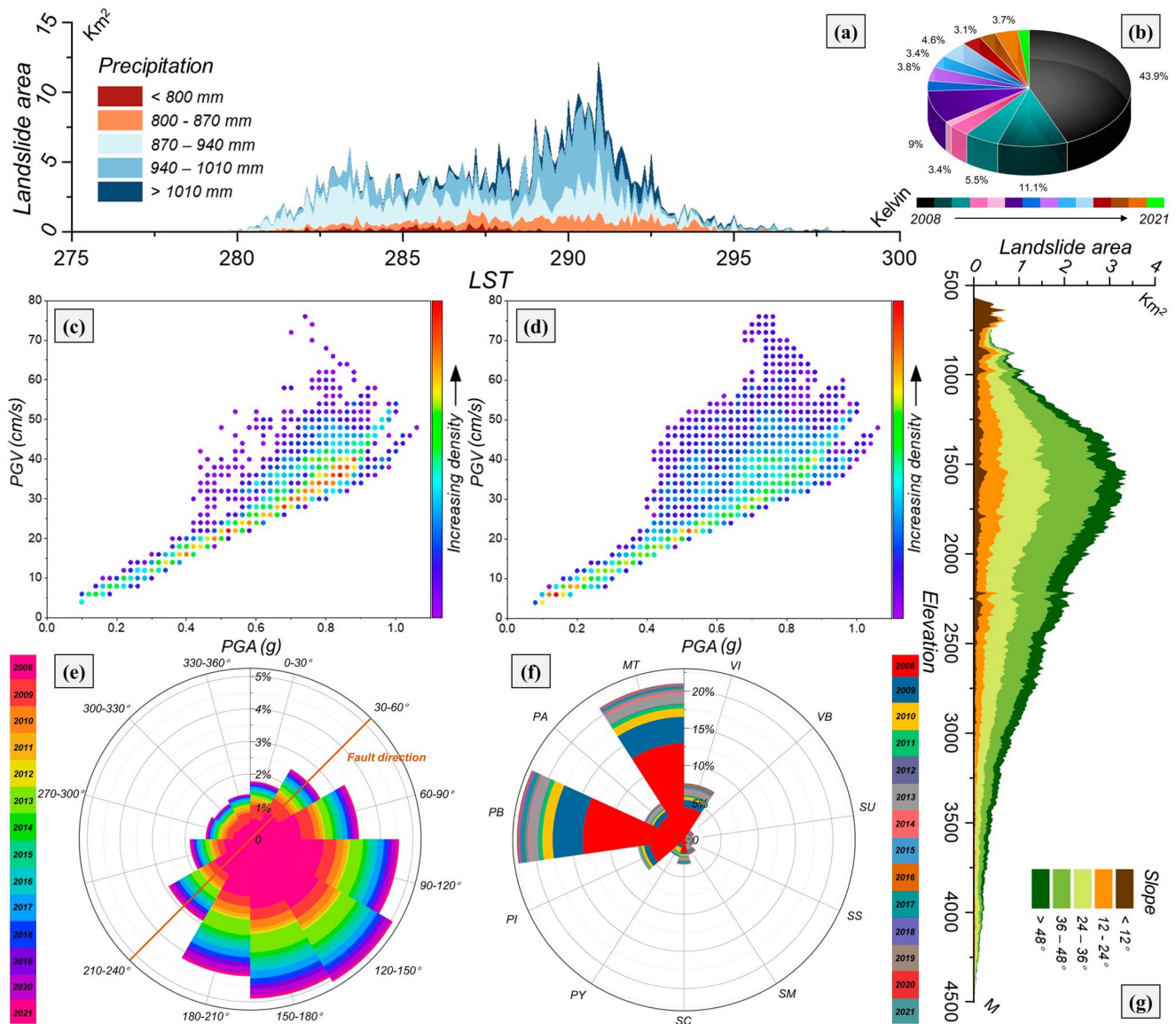


Figure 3. Post-earthquake landslide patterns and evolutions. (a) Post-earthquake landslide distribution under different climatic conditions. (b) Annual proportion of post-earthquake landslides; Distribution of (c) co-seismic and (d) post-seismic landslides under different ground shaking intensity; Annual distribution of post-earthquake landslides with different (e) aspects and (f) lithologies (VB, Basic Volcanic Rocks; SU, Unconsolidated Sediments; SS, Siliciclastic Sedimentary Rocks; SM, Mixed Sedimentary Rocks; SC, Carbonate Sedimentary Rocks; PY, Pyroclastics); (g) Distribution of post-earthquake landslides under different topographic factors.

curve of landslide areas within such a broad range and a long-time scale, the fluctuation of this point does not significantly deflect the subsequent recovery fitting of descending trend.

4.2. Post-Earthquake Landslide Evolution

Through the annual statistics of post-earthquake landslide area, it can be concluded that the co-seismic landslide area in 2008 constituted a significant portion, precisely 43.9%, of the overall landslide area during the 14-year period following the earthquake. Conversely, the long-term cumulative landslide area after the earthquake comprised 56.1% of the total, as illustrated in Figure 3b. In order to investigate the impact of seismic ground shaking on triggering landslides, the PGA and PGV distributions of landslide records in 2008 and 2009–2021 were separately analyzed. The scatter density comparison in Figures 3c and 3d demonstrates that co-seismic landslides exhibit high PGA and PGV ($PGA > 0.4$ g and $PGV > 15$ cm/s), while post-seismic landslides are evenly distributed in the seismic range of all intensities. This finding suggests that co-seismic landslides

responded instantly to strong seismic stress during the mainshocks. Conversely, co-seismic debris deposited at higher seismic intensities as well as cracked mountains with weakened rigidity at lower seismic intensities served as the source materials of successive post-seismic landslides and debris flows. These subsequent events were influenced by other forces (e.g., rainfall) after the earthquake rather than the intensity of co-seismic ground shaking (Song et al., 2022).

An analysis of post-earthquake landslides under varying climatic conditions was carried out, and the results are exhibited in Figure 3a. The relationship between landslide area and LST follows an approximate Generalized Gaussian Distribution (GGD), with a mean of 288.65 K and a standard deviation of 7.93 K. The majority of landslides occurred at temperatures ranging from 280.73 to 296.58 K. Through further analysis that incorporated precipitation, it was found that landslide area with high precipitations (>940 mm) was greater than that with low precipitations (<870 mm) at all LSTs. In addition, it was observed that the proportion of light precipitation-related (<800 mm) landslides was small in high LSTs (>289 K), while it significantly increased in regions with low temperatures (<289 K). The soil textures and vegetation types in hot regions result in higher saturated soil water content (SSWC), requiring heavier rainfall to induce sliding. Conversely, the SSWC decrease under low LSTs, and a minor rainfall is capable of triggering slope instability (Gariano & Guzzetti, 2016; Huggel et al., 2012; Lehmann et al., 2013). Similarly, the topographic effects of altitude and slope were also analyzed, as demonstrated in Figure 3g. The relationship between post-earthquake landslide area and altitude also follows an approximate GGD with a mean of 1810.93 m and a standard deviation of 1178.29 m. Hence, the landslides mainly occurred between 632.64 and 2989.21 m. Combined with the derived slope information, it was observed that the landslide area in steep slopes (>36°) is greater than that of gentle slopes (<24°) at all altitudes, but the proportion of gentle-slope landslides in low-altitude (<1,000 m) areas is higher than that in high-altitude (>1,000 m) areas. Our on-site investigation reveals that the abnormal dominance of gentle-slope landslides between the lowest to ~750 m, where human activities are more frequent than the mountainous region, is partially caused by the insufficient removal of anthropogenic disturbances, such as cropland cultivation, road development, and building construction. Furthermore, low altitudes tend to accumulate loose materials produced by the earthquake, resulting in gentle-slope deposits, where shallow landslides easily respond to rainfall (Cui et al., 2014; C. Li et al., 2018). However, scarce sources make it difficult to store deposits at high altitudes. Steep slopes that disintegrated under the action of gravity or external forces were the bulk of high-altitude landslides.

In addition to altitude and slope, the pattern of post-earthquake landslides on different aspects were also investigated. Figure 3e showcases the annual landslide areas across different aspects, highlighting the evident predominance of the southeast direction, which can be attributed to the compounding impacts: (a) The directivity of causative rupture movement and seismic wave propagation contributed a notable effect to the aspect of co-seismic landslides. The dominant sliding direction (southeast) of landslides closely aligns with the thrust direction of BYF (Qi et al., 2010; Xu et al., 2014); (b) The study area is influenced by the southeast monsoon, and the consequential severe weathering rendered slopes on these aspects more susceptible to external forces (Yang et al., 2018). The distribution of post-earthquake landslides varied across different lithologies, as depicted in Figure 3f. Metamorphics (MT) and Basic Plutonic Rocks (PB) constituted the primary lithologies associated with landslides, followed by Intermediate Volcanic Rocks (VI), Intermediate Plutonic Rocks (PI), and Acid Plutonic Rocks (PA). On one hand, the uneven distribution of lithology within the study area serves as a significant contributing factor to this phenomenon. On the other hand, lithology itself exerts a substantial influence on the shear resistance of slope structure. Slope bedrock composed of lithologies with higher cohesive strength possesses the capacity of withstanding external forces and mitigating the occurrence of shallow landslides, whereas lithologies with lesser cohesive strength exhibit the opposite effects (Frattini & Crosta, 2013; Gallen et al., 2015; Stark & Guzzetti, 2009).

Besides, to further access change patterns of post-earthquake landslides, the annual landslides under varying environmental conditions were analyzed, and a comprehensive exposition was conducted combining Text S2 and Figure S5 in Supporting Information S1.

4.3. Post-Earthquake Ecological Restoration

Following the Wenchuan earthquake, the occurrence of post-earthquake landslides gradually decreased until reaching a state of stabilization. The scatters of annual landslide areas with an exponential function were fitted, as depicted in Figure 4a. The high R-square value of 0.97 and the p-value, which is significantly lower than 0.01,

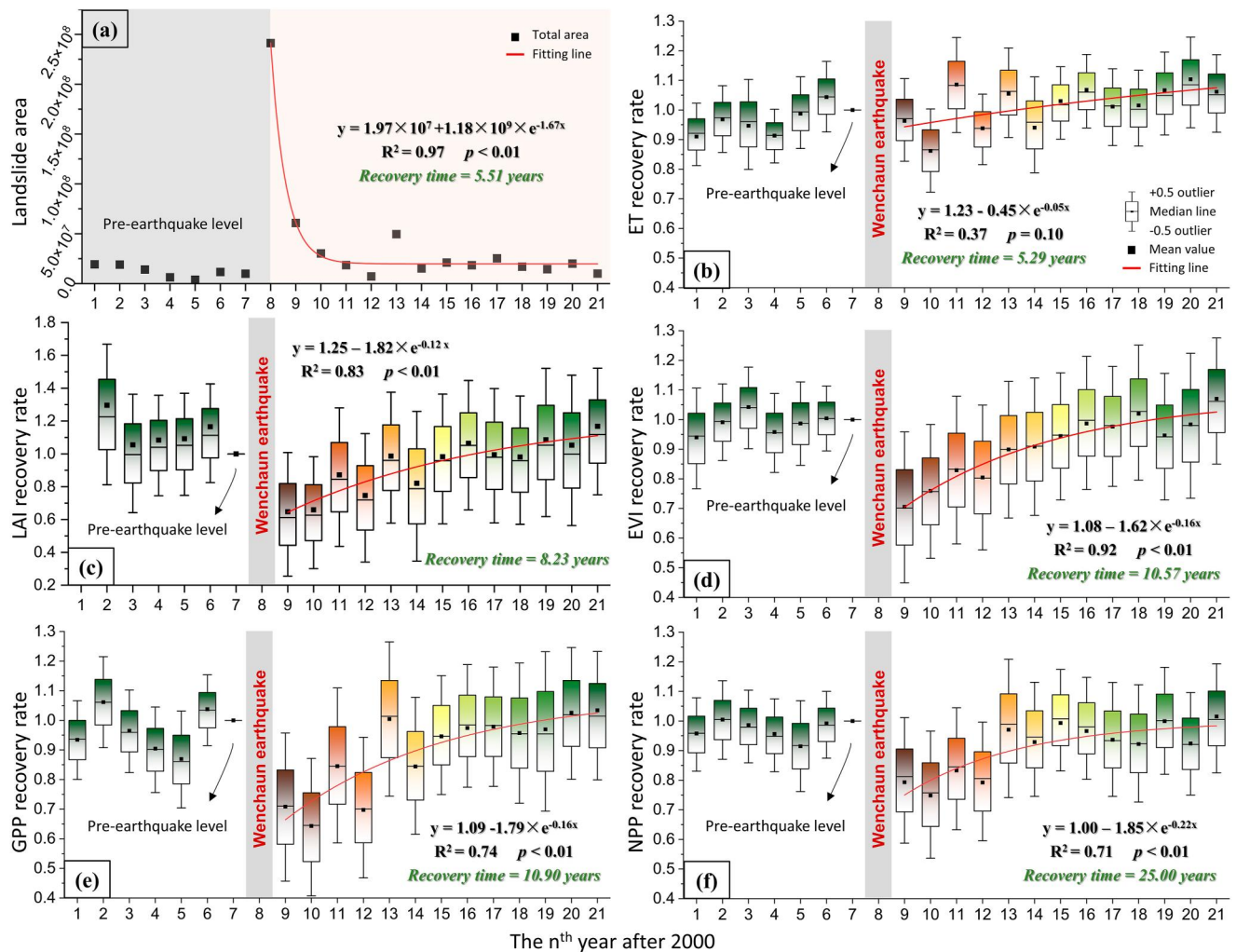


Figure 4. Long-term restoration of land surface process after the Wenchuan earthquake. (a) Attenuation of landslide activity. Ecological restoration with the indicators of (b) ET, (c) leaf area index, (d) EVI, (e) gross primary productivity, and (f) net primary productivity, respectively.

serve as a testament to the reliability of the fitting model. In accordance with the restoration criteria proposed by Viedma et al. (1997), a year is deemed to have returned to its pre-earthquake level when the activated landslide area has decayed beyond 99.99% of the difference between the maximum and the convergent minimum. By combining the fitting model with the restoration criteria, it can be asserted that it took 5.51 years for post-earthquake landslide activity to return to its pre-earthquake level.

Despite the rapid return of landslide activity to its former state, the damage inflicted upon terrestrial ecology due to land surface changes may require longer periods to subside. Hence, we selected crucial indicators, including ET, LAI, EVI, GPP, and NPP, for ecological restoration analysis. Since the unit of these indicators is the percentage of the corresponding pixel value a year before the earthquake, the time required for recovery can be determined when the variable prediction of the fitting curve reaches 100% after the earthquake. ET represents the combined process of soil and water evaporation as well as plant transpiration. Landslides damaged soil and vegetation and changed surface and subsurface runoff, inevitably impacting ET. According to the fitting model, it took 5.29 years for ET to revert to its pre-earthquake level. This duration is in close proximity to that required for the landslide restabilization, thereby confirming the stability of landscape pattern at the same time. However, the insignificance of its R-square and p-value suggests its recuperation is susceptible to extraneous factors. LAI and EVI measure leaf area and greenness, respectively, which are both crucial characterizations of land surface vegetation. The results indicate that the recovery times of LAI and EVI were 8.23 and 10.57 years, respectively. The regrowth and succession of vegetation require a longer process compared to inorganic landslides. It has also

been observed that LAI and EVI exhibit greater variability in scatter than ET. This implies changes in comprehensive ET are less pronounced as compared to vegetation indices, suggesting alterations in vegetation are just partial contributors to the fluctuation of ET. GPP and NPP measure the total amount of carbon compounds produced by plant photosynthesis in an ecosystem. Their annual scatters were calculated and fitted after the earthquake. The results reveal that the recovery of GPP requires 10.90 years, which is 2.67 and 0.33 years more than those of LAI and EVI, respectively. Furthermore, NPP would not restore to its original level until 25.00 years after the earthquake, which is 16.77 and 14.43 years more than those of LAI and EVI, respectively. The ecological functions of vegetation (e.g., carbon source and sink) require a longer recovery period than plant growth. Therefore, the impact of post-earthquake landslides on terrestrial ecology is much more profound. It can also be inferred from these results that landslides initiated by strong earthquakes worldwide deeply influence carbon storage and balance between land surface and atmosphere, thereby having considerable impacts on global climate change (Frith et al., 2018).

5. Conclusions

To explore the long-term evolution and restoration of post-earthquake landslides following the Wenchuan earthquake, we devised a groundbreaking framework for continuous landslide detection via time-series remote sensing images. Our research achieved the recognition of landslides in the affected region for over 21 years prior to and following the earthquake, providing the most comprehensive landslide activities to date. Leveraging the identified landslide information, we uncovered the key patterns of post-earthquake landslide evolution. Notably, significant discrepancies in post-earthquake landslide activities were observed under varying conditions of topographic, lithologic, seismic, and climatic factors. In addition to tracking the decrease of post-earthquake landslides, we also conducted a comprehensive analysis of important ecological indicators. The results reveal that the recovery of plant growth required more time than that of landslide activity, while the restoration of vegetation carbon sequestration experienced even lengthier periods.

Data Availability Statement

Surface reflectance is acquired from Landsat 5, 7, and 8 images, courtesy of the U.S. Geological Survey. DEM is provided by NASADEM (Crippen et al., 2016). Lithology is achieved from Global Lithological Map (Hartmann & Moosdorf, 2012). PGA and PGV of the Wenchuan earthquake are obtained from ShakeMap (Wald et al., 2022). Precipitation is provided by CHIRPS (Funk et al., 2015). LST, ET, LAI, EVI, GPP, and NPP are all obtained from MODIS products (Didan, 2021; Myneni et al., 2021; Running & Zhao, 2019; Running et al., 2015, 2017; Wan et al., 2021). The land cover data sets which we considered for training sample collection in CCDC are provided by Gong et al. (2019), Zanaga et al. (2021), and X. Zhang et al. (2021). The time-series landslide detection approach is modified based on CCDC algorithm, which is provided by Zhu and Woodcock (2014). The time-series landslide detection achievements are released in Wang et al. (2023).

Acknowledgments

The research is supported by the National Science Fund for Distinguished Young Scholars of China (Grant 42125702), the National Natural Science Foundation of China (Grant 42307263), the New Cornerstone Science Foundation through the XPLOER PRIZE (Grant XPLOER-2022-1012), and the Natural Science Foundation of Sichuan Province (Grants 2022NSFSC0003 and 2022NSFSC1083).

References

- Chen, M., Tang, C., Xiong, J., Shi, Q., Li, N., Gong, L., et al. (2020). The long-term evolution of landslide activity near the epicentral area of the 2008 Wenchuan earthquake in China. *Geomorphology*, 367, 107317. <https://doi.org/10.1016/j.geomorph.2020.107317>
- Crippen, R., Buckley, S., Agram, P., Belz, E., Gurrola, E., Hensley, S., et al. (2016). NASADEM global elevation model: Methods and progress [Dataset]. The International Archives of the Photogrammetry, Remote Sensing and Spatial Information Sciences, 41, 125–128. <https://doi.org/10.5194/isprs-archives-XLI-B4-125-2016>
- Cruden, D. M. (1991). A simple definition of a landslide. *Bulletin of the International Association of Engineering Geology-Bulletin de l'Association Internationale de Géologie de l'Ingénieur*, 43(1), 27–29. <https://doi.org/10.1007/BF02590167>
- Cui, P., Guo, C.-X., Zhou, J.-W., Hao, M.-H., & Xu, F.-G. (2014). The mechanisms behind shallow failures in slopes comprised of landslide deposits. *Engineering Geology*, 180, 34–44. <https://doi.org/10.1016/j.enggeo.2014.04.009>
- Dai, F., Tu, X., Xu, C., Gong, Q., & Yao, X. (2011). Rock avalanches triggered by oblique-thrusting during the 12 May 2008 Ms 8.0 Wenchuan earthquake, China. *Geomorphology*, 132(3–4), 300–318. <https://doi.org/10.1016/j.geomorph.2011.05.016>
- Didan, K. (2021). MODIS/Terra Vegetation Indices 16-Day L3 Global 250m SIN Grid V061 [Dataset]. NASA EOSDIS Land Processes Distributed Active Archive Center. <https://doi.org/10.5067/MODIS/MOD13Q1.061>
- Fan, X., Scaringi, G., Domènech, G., Yang, F., Guo, X., Dai, L., et al. (2019). Two multi-temporal datasets that track the enhanced landsliding after the 2008 Wenchuan earthquake. *Earth System Science Data*, 11(1), 35–55. <https://doi.org/10.5194/essd-11-35-2019>
- Fan, X., Scaringi, G., Korup, O., West, A. J., van Westen, C. J., Tanyas, H., et al. (2019). Earthquake-induced chains of geologic hazards: Patterns, mechanisms, and impacts. *Reviews of Geophysics*, 57(2), 421–503. <https://doi.org/10.1029/2018RG000626>
- Fan, X., Yunus, A. P., Scaringi, G., Catani, F., Siva Subramanian, S., Xu, Q., & Huang, R. (2021). Rapidly evolving controls of landslides after a strong earthquake and implications for hazard assessments. *Geophysical Research Letters*, 48(1), e2020GL090509. <https://doi.org/10.1029/2020GL090509>

- Frattini, P., & Crosta, G. B. (2013). The role of material properties and landscape morphology on landslide size distributions. *Earth and Planetary Science Letters*, 361, 310–319. <https://doi.org/10.1016/j.epsl.2012.10.029>
- Frith, N. V., Hilton, R. G., Howarth, J. D., Gröcke, D. R., Fitzsimons, S. J., Croissant, T., et al. (2018). Carbon export from mountain forests enhanced by earthquake-triggered landslides over millennia. *Nature Geoscience*, 11(10), 772–776. <https://doi.org/10.1038/s41561-018-0216-3>
- Funk, C., Peterson, P., Landsfeld, M., Pedreros, D., Verdin, J., Shukla, S., et al. (2015). The climate hazards infrared precipitation with stations—A new environmental record for monitoring extremes [Dataset]. Scientific Data, 2(1), 1–21. <https://doi.org/10.1038/sdata.2015.66>
- Gallen, S. F., Clark, M. K., & Godt, J. W. (2015). Coseismic landslides reveal near-surface rock strength in a high-relief, tectonically active setting. *Geology*, 43(1), 11–14. <https://doi.org/10.1130/G36080.1>
- Gariano, S. L., & Guzzetti, F. (2016). Landslides in a changing climate. *Earth-Science Reviews*, 162, 227–252. <https://doi.org/10.1016/j.earscirev.2016.08.011>
- Gong, P., Liu, H., Zhang, M., Li, C., Wang, J., Huang, H., et al. (2019). Stable classification with limited sample: Transferring a 30-m resolution sample set collected in 2015 to mapping 10-m resolution global land cover in 2017 [Dataset]. Science Bulletin, 64(6), 370–373. <https://doi.org/10.1016/j.scib.2019.03.002>
- Gorelick, N., Hancher, M., Dixon, M., Ilyushchenko, S., Thau, D., & Moore, R. (2017). Google Earth Engine: Planetary-scale geospatial analysis for everyone. *Remote Sensing of Environment*, 202, 18–27. <https://doi.org/10.1016/j.rse.2017.06.031>
- Guzzetti, F., Carrara, A., Cardinali, M., & Reichenbach, P. (1999). Landslide hazard evaluation: A review of current techniques and their application in a multi-scale study, Central Italy. *Geomorphology*, 31(1–4), 181–216. [https://doi.org/10.1016/S0169-555X\(99\)00078-1](https://doi.org/10.1016/S0169-555X(99)00078-1)
- Hartmann, J., & Moosdorf, N. (2012). The new global lithological map database GLiM: A representation of rock properties at the Earth surface [Dataset]. *Geochemistry, Geophysics, Geosystems*, 13(12). <https://doi.org/10.1029/2012GC004370>
- Hovius, N., Meunier, P., Lin, C.-W., Chen, H., Chen, Y.-G., Dadson, S., et al. (2011). Prolonged seismically induced erosion and the mass balance of a large earthquake. *Earth and Planetary Science Letters*, 304(3–4), 347–355. <https://doi.org/10.1016/j.epsl.2011.02.005>
- Hu, W., Scaringi, G., Xu, Q., & Huang, R. (2018). Internal erosion controls failure and runoff of loose granular deposits: Evidence from flume tests and implications for postseismic slope healing. *Geophysical Research Letters*, 45(11), 5518–5527. <https://doi.org/10.1029/2018GL078030>
- Huang, R., & Fan, X. (2013). The landslide story. *Nature Geoscience*, 6(5), 325–326. <https://doi.org/10.1038/ngeo1806>
- Huggel, C., Clague, J. J., & Korup, O. (2012). Is climate change responsible for changing landslide activity in high mountains? *Earth Surface Processes and Landforms*, 37(1), 77–91. <https://doi.org/10.1002/esp.2223>
- Kincey, M. E., Rosser, N. J., Robinson, T. R., Densmore, A. L., Shrestha, R., Pujara, D. S., et al. (2021). Evolution of coseismic and post-seismic landsliding after the 2015 Mw 7.8 Gorkha earthquake, Nepal. *Journal of Geophysical Research: Earth Surface*, 126(3), e2020JF005803. <https://doi.org/10.1029/2020JF005803>
- Korup, O., Densmore, A. L., & Schlunegger, F. (2010). The role of landslides in mountain range evolution. *Geomorphology*, 120(1–2), 77–90. <https://doi.org/10.1016/j.geomorph.2009.09.017>
- LaHusen, S. R., Duvall, A. R., Booth, A. M., Grant, A., Mishkin, B. A., Montgomery, D. R., et al. (2020). Rainfall triggers more deep-seated landslides than Cascadia earthquakes in the Oregon Coast Range, USA. *Science Advances*, 6(38), eaba6790. <https://doi.org/10.1126/sciadv.aba6790>
- Lehmann, P., Gambazzi, F., Suski, B., Baron, L., Askarinejad, A., Springman, S. M., et al. (2013). Evolution of soil wetting patterns preceding a hydrologically induced landslide inferred from electrical resistivity survey and point measurements of volumetric water content and pore water pressure. *Water Resources Research*, 49(12), 7992–8004. <https://doi.org/10.1002/2013WR014560>
- Li, C., Wang, M., & Liu, K. (2018). A decadal evolution of landslides and debris flows after the Wenchuan earthquake. *Geomorphology*, 323, 1–12. <https://doi.org/10.1016/j.geomorph.2018.09.010>
- Li, G. K., & Moon, S. (2021). Topographic stress control on bedrock landslide size. *Nature Geoscience*, 14(5), 307–313. <https://doi.org/10.1038/s41561-021-00739-8>
- Lin, W.-T., Chou, W.-C., Lin, C.-Y., Huang, P.-H., & Tsai, J.-S. (2005). Vegetation recovery monitoring and assessment at landslides caused by earthquake in Central Taiwan. *Forest Ecology and Management*, 210(1–3), 55–66. <https://doi.org/10.1016/j.foreco.2005.02.026>
- Marc, O., Hovius, N., Meunier, P., Uchida, T., & Hayashi, S. (2015). Transient changes of landslide rates after earthquakes. *Geology*, 43(10), 883–886. <https://doi.org/10.1130/G36961.1>
- Metternicht, G., Hurni, L., & Gogu, R. (2005). Remote sensing of landslides: An analysis of the potential contribution to geo-spatial systems for hazard assessment in mountainous environments. *Remote Sensing of Environment*, 98(2–3), 284–303. <https://doi.org/10.1016/j.rse.2005.08.004>
- Myneni, R., Knyazikhin, Y., & Park, T. (2021). MODIS/Terra Leaf Area Index/FPAR 8-Day L4 Global 500m SIN Grid V061 [Dataset]. NASA EOSDIS Land Processes Distributed Active Archive Center. <https://doi.org/10.5067/MODIS/MOD15A2H.061>
- Qi, S., Xu, Q., Lan, H., Zhang, B., & Liu, J. (2010). Spatial distribution analysis of landslides triggered by 2008.5. 12 Wenchuan Earthquake, China. *Engineering Geology*, 116(1–2), 95–108. <https://doi.org/10.1016/j.enggeo.2010.07.011>
- Rasigraf, O., & Wagner, D. (2022). Landslides: An emerging model for ecosystem and soil chronosequence research. *Earth-Science Reviews*, 231, 104064. <https://doi.org/10.1016/j.earscirev.2022.104064>
- Running, S., Mu, Q., & Zhao, M. (2015). MOD17A2H MODIS/Terra Gross Primary Productivity 8-Day L4 Global 500m SIN Grid V006 [Dataset]. NASA EOSDIS Land Processes Distributed Active Archive Center. <https://doi.org/10.5067/MODIS/MOD17A2H.006>
- Running, S., Mu, Q., & Zhao, M. (2017). MOD16A2 MODIS/Terra Net Evapotranspiration 8-Day L4 Global 500m SIN Grid V006 [Dataset]. NASA EOSDIS Land Processes Distributed Active Archive Center. <https://doi.org/10.5067/MODIS/MOD16A2.006>
- Running, S., & Zhao, M. (2019). MOD17A3HGF MODIS/Terra Net Primary Production Gap-Filled Yearly L4 Global 500 m SIN Grid V006 [Dataset]. NASA EOSDIS Land Processes Distributed Active Archive Center. <https://doi.org/10.5067/MODIS/MOD17A3HGF.006>
- Shen, P., Zhang, L. M., Fan, R., Zhu, H., & Zhang, S. (2020). Declining geohazard activity with vegetation recovery during first ten years after the 2008 Wenchuan earthquake. *Geomorphology*, 352, 106989. <https://doi.org/10.1016/j.geomorph.2019.106989>
- Sidle, R. C., & Bogaard, T. A. (2016). Dynamic earth system and ecological controls of rainfall-initiated landslides. *Earth-Science Reviews*, 159, 275–291. <https://doi.org/10.1016/j.earscirev.2016.05.013>
- Song, C., Yu, C., Li, Z., Utili, S., Frattini, P., Crosta, G., & Peng, J. (2022). Triggering and recovery of earthquake accelerated landslides in Central Italy revealed by satellite radar observations. *Nature Communications*, 13(1), 7278. <https://doi.org/10.1038/s41467-022-35035-5>
- Stark, C., & Guzzetti, F. (2009). Landslide rupture and the probability distribution of mobilized debris volumes. *Journal of Geophysical Research*, 114(F2), F00A02. <https://doi.org/10.1029/2008JF001008>
- Tang, C., Van Westen, C. J., Tanyas, H., & Jetten, V. G. (2016). Analysing post-earthquake landslide activity using multi-temporal landslide inventories near the epicentral area of the 2008 Wenchuan earthquake. *Natural Hazards and Earth System Sciences*, 16(12), 2641–2655. <https://doi.org/10.5194/nhess-16-2641-2016>